Rock Mechanics and Rock Engineering (2026) 59:5839–5856
https://doi.org/10.1007/s00603-024-03978-4

ORIGINAL PAPER

Numerical Modelling of the Influence of Tidal Stresses on Fracture Patterns on the Surface of Europa

John C. Walding[1] · Adriana Paluszny[1] · Robert W. Zimmerman[1]

Received: 22 December 2023 / Accepted: 1 May 2024 / Published online: 10 June 2024
© The Author(s) 2024

Abstract

Jupiter's satellite Europa is covered by an ice shell exhibiting many surface features, including linear structures called lineae, which in this work are treated as fractures. A three-dimensional finite-element simulator is used to numerically model fracture nucleation, growth, and interaction, assuming the ice is an isotropic, linear elastic medium. Tidal stresses are exerted upon the ice through the Jovian orbital relationship. These stresses are calculated using a closed-form model derived from first principles. The fractures grow in response to stress concentration around their tips, and a damage criterion models the weakening of the ice matrix. Three-dimensional non-planar multiple fracture growth is modelled as a function of geometric multi-modal stress intensity factors computed at the fracture tips. Fracturing is evaluated over multi-scale periods, from days to millions of years, thus capturing multiple tidal effects. Fracture behaviour is modelled across the Europan surface in one domain. The patterns are dense clusters of lineae about the stress maxima with diffuse fracturing in outlying regions. Fractures are also modelled in the vicinity of subsurface meltwater lenses, where fractures form parallel to the surface in contrast to the usual perpendicular orientation. The resultant fracture patterns are qualitatively compared against images from NASA's Galileo mission. This work contributes to the understanding of Europan lineae by illustrating how they behave in a fracture mechanics framework, and suggests interesting results regarding lineae interaction with meltwater lenses. This work is also a proof of concept for this modelling approach, and will serve as the framework for future work.

Highlights

- A tidal stress model is paired with a finite element fracture simulator to model Lineae as fractures driven by tidal stresses on the Europan surface.
- Clusters of fractures which are normal to the surface nucleate and grow primarily around the Equatorial regions.
- In the regions above subsurface meltwater lenses fractures grow parallel to the surface.
- There is qualitative correlation between simulation results and observed lineae.

Keywords Europa · Fracture growth · Tidal stresses · Finite element method · Ice · Planetary rock mechanics

1 Introduction

The sixth closest of all moons and smallest of the Galilean moons of Jupiter, Europa has a radius of 1560 km (Nimmo et al. 2007), the majority of which is taken by the silicate core. Surrounding the silicate core is believed to be a vast, contiguous liquid water oceanic layer (Carr et al. 1998), itself encased by a water ice shell, which forms the Europan surface. The oceanic layer is generally understood to be approximately 100 km thick (Pappalardo et al. 1999),

✉ John C. Walding
john.walding15@imperial.ac.uk

[1] Department of Earth Science and Engineering, Imperial College London, London, UK

whereas there is less consensus on the thickness of the ice crust. It is estimated to be between 1 and 30 km thick (Billings and Kattenhorn 2005), with the lower estimates drawn from analysis of the mechanical flexure of the ice (Figueredo et al. 2002; Nimmo et al. 2007), and the higher estimates based on a thermodynamic analysis of the crust (Hussmann et al. 2002; McKinnon 1999; Ojakangas and Stevenson 1989), with analyses of surface impact cratering yielding intermediate values (Greeley et al. 1998; Moore et al. 1998; Schenk 2002).

Tidal flexing due to the obliquity of Europa's orbit around Jupiter heats the Europan silicate core (Cassen et al. 1979), which combined with the ice crust acting as a lid, allows the subsurface ocean to remain liquid and maintain potentially habitable conditions. As a result, Europa is seen as a primary candidate for harbouring extraterrestrial life (Schulze-Makuch and Irwin 2001; Kargel et al. 2000; Greenberg et al. 2000), and consequently the ocean-ice system is of great scientific curiosity.

The distance between Earth and the Jovian system restricts the possible observation of Europa by terrestrial telescopes. Fortunately, the icy surface of Europa has been observed by multiple NASA missions to the outer solar system (Pioneers 1 and 2, Voyagers 1 and 2, Galileo, New Horizons and Juno), which have yielded many images across the surface, although with variable quality. The upcoming Europa Clipper mission is, however, the first mission that is principally concerned with Europa, promising to provide a much higher resolution representation of the surface (Bayer et al. 2019). However, with the Clipper aiming to arrive at Europa in 2030, in the interim the existing images must be used; in the present work, the main source of observational data is the Galileo mission. These images reveal what is thought to be the youngest and smoothest surface of any body in the solar system. The surface smoothness is likely to be due to resurfacing (Leonard et al. 2018), with a period of 20–180 million years. Nevertheless, the surface exhibits many notable features. These features can be classified into three broad categories; approximately circular uplifts and depressions called *Lenticulae* (Culha and Manga 2016), *Chaos* regions (Leonard et al. 2022), characterised by particularly jagged and broken terrain (Collins and Nimmo 2009), and *Lineae*, the focus of this work, which are linear features that cross the Europan surface at multiple scales from minor 100 m features to moon-spanning 1000 km long features. These features are theorised to be either active fractures or structures that were initially fractures in the ice crust (Helfenstein and Parmentier 1983).

If the lineae are in fact fractures (where the term 'fracture' will be used here to denote any discontinuity in the ice matrix, open or closed, that may develop in response to stress concentration), then they are thought to exist due to the presence of subsurface liquid water (Pappalardo et al. 1999; Carr et al. 1998).

Work previously conducted has used Linear Elastic Fracture Mechanics (LEFM) methods to investigate fracturing of the Europan crust concerning different aspects of the system, including cycloidal features (Marshall and Kattenhorn 2005; Poinelli et al. 2019) or the presence of subsurface water sills (Craft et al. 2016). In particular, Lee et al. (2005) discussed the capacity for vertical penetration of surface fractures, concluding that total crust penetration to the oceanic layer is feasible. This is disputed by Qin et al. (2007), who posited that normal stresses upon the fractures were insufficiently considered, and that this correction would prevent fractures from penetrating to the ocean. Vertical fracture propagation was further investigated by Rudolph and Manga (2009) and Walker et al. (2021), who concluded that total penetration was unlikely. Rudolph and Manga (2009) reported that penetration was only viable for crust thicknesses less than 2.5 km, which is below most estimates. The work undertaken in Trumbo and Brown (2023) and Carnahan et al. (2022) further suggest that surface-ocean interaction is present, though through alternate methodology. Trumbo and Brown (2023) posits that surface CO_2 serves as indirect evidence of surface-ocean linkage, while Carnahan et al. (2022) suggests post impact viscous deformation may lead to sustained surface-ocean exchange. In summation it is presently disputed whether fractures can penetrate to the ocean.

In this work, the nucleation and propagation of Europan surface fractures in response to Jovian tidal forcing is modelled in multiple temporal regimes, using a first-principles fracture mechanics growth model, with geometric representation of individual fractures, combining damage-informed fracture nucleation and energy-based fracture growth simulation. In doing so, this work aims to help ascertain whether Europan lineae are fracture-like features, and to then also further investigate the lineae's large-scale behaviour.

2 Methodology

2.1 Tidal Stress Model

Deformation of the Europan crust, and therefore the growth of fractures in the crust, is presently thought to be primarily a consequence of the tidal stresses resulting from Europa's orbit around Jupiter (Helfenstein and Parmentier 1983). Therefore, the stresses driving the fracture growth model are computed with a tidal stress model, first conceived by Wahr et al. (2009).

The tidal stress model incorporates two stressors: diurnal tides, and Non-Synchronous Rotation (NSR). Other sources of tidal stress are possible, such as orbital obliquity (Bills 2005; Rhoden et al. 2011), or liberational tides (Van Hoolst

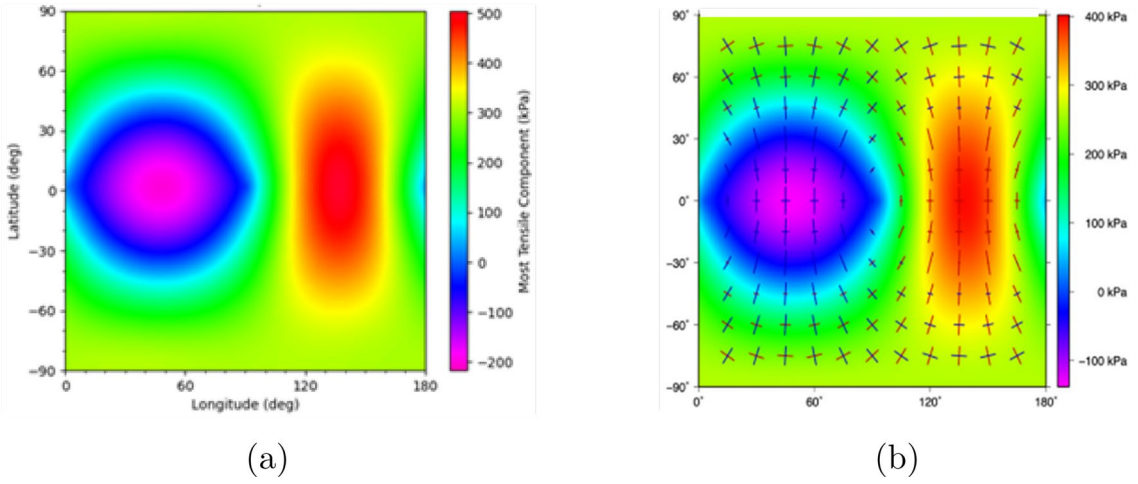


Fig. 1 Tidal stress fields for one hemisphere of the Europan surface. The two hemispheres' stress fields are identical. **a** The result from the current implementation. The scalar field corresponds to the most-tensile component of the stress tensor. **b** The same field from Wahr et al. (2009). Strong correlation between the two is observed

et al. 2008). These, however, are assumed to be second-order effects by Wahr et al. (2009), and this assumption is maintained in the present work. It is, however, worth noting that the analytical form of the tidal stress solution is readily amenable to the inclusion of further stressors, with more recent literature supporting the non-negligibility of these effects (Rhoden et al. 2010; Rhoden and Hurford 2013).

The diurnal tides are a consequence of Europa's orbital eccentricity, and exert stresses of approximate magnitude 100 kPa, where the stress field has a period of one Europan day, defined as one orbit around Jupiter (3.5 Earth days), with rate f_{diurnal}. NSR stresses (McEwen 1986) only arise due to the presence of a contiguous subsurface ocean, which mechanically decouples the crust from the silicate core. Even though the core is tidally locked, the free floating crust is able to rotate at a slightly different rate, $f_{\text{diurnal}} + f_{\text{NSR}}$, where f_{NSR} is the NSR rate. The NSR period on Europa is estimated to be between 10^5 and 10^9 years (Geissler et al. 1998). As the crust is rotating with respect to the parent body, the tidal bulge (Melosh 1980) passes across the surface and imparts stress in doing so. The resultant NSR stress is dependent on both f_{NSR} and the viscosity of the ice, with possible values from 0 Pa to 3 MPa.

The tidal stresses are calculated using a model based upon the theory developed by Wahr et al. (2009). This model uses the base gravitational potential to derive closed-form analytical expressions for tidal stress exerted upon the surface, given a location and a time, where the time is measured from Europan periapsis (the closest approach of Europa to Jupiter).

The model assumes a four-layered Maxwell solid (Jaeger et al. 2007) structure for Europa, consisting of the silicate core, an oceanic layer of liquid water, followed by the ice crust itself divided into an inner viscoelastic, warm and ductile layer (hereafter the ductile layer) and an outer cold, brittle layer (hereafter the brittle layer). The model returns the stress tensor, τ, though given the context there are no stresses in the r direction, leaving only $\tau_{\theta\theta}$, $\tau_{\phi\phi}$ and $\tau_{\theta\phi} = \tau_{\phi\theta}$.

The tidal stresses fields as generated by the present implementation are shown in Fig. 1, with the stresses generated by Wahr et al. (2009) shown for comparison.

The base model only yields the surface stress, however, whereas the present work requires knowledge of the stress at depth. To this end, the stress at a point on the surface is multiplied by a simple factor F_{Depth}, defined as

$$F_{\text{Depth}} = \frac{r}{R_{\text{Europa}}} \tag{1}$$

where r is the radial value at a given depth and R_{Europa} is the outer radius of Europa (see Table 1).

2.2 Fracture Model

This work uses the Imperial College Geomechanics Toolkit (ICGT) (Thomas et al. 2020) as the fracture simulator. The following section describes its operation pertinent to its usage in this context.

2.2.1 Mechanical Deformation

The mechanical deformation of the ice matrix in response to tidal stresses is computed in a three-dimensional volumetric domain using a linear-elastic finite element model (Cook et al. 2007). This calculation assumes that the brittle ice layer behaves as a linear elastic and isotropic material,

which is expected for ice at the temperatures found on the Europan surface, which are estimated to be 110 K at the equator, and 50 K at the poles (Ashkenazy 2019). Under these assumptions the stress and strain are governed as

$$\sigma = \mathbf{D}(\varepsilon - \varepsilon_0) + \sigma_0 \tag{2}$$

where σ is the Cauchy stress tensor, ε is the infinitesimal strain tensor, $\mathbf{D}$ is the linear elastic stiffness matrix, and σ_0 and ε_0 are the initial stress and strain respectively. The force balance of this system is then as follows

$$\underline{\delta}\sigma + F = 0 \tag{3}$$

where $\underline{\delta}$ is the differential matrix operator and F is the summation of all body forces exerted upon the object.

2.2.2 Fracture Nucleation

The initial state of the domain in the simulation is homogeneous and isotropic, barring certain simulation exceptions (see Sect. 3.3.2). Fractures may either be inserted into the domain with either prescribed locations or a probabilistic distribution, or be nucleated in accordance to the mechanical state of the ice. The present work uses the geomechanical computation method.

In this method, the equivalent strain $\widetilde{\varepsilon}$ is used to determine the locations for new fractures in accordance to the approach developed by Mazars et al. (2015). The nucleation sites are selected to be those locations at which $\widetilde{\varepsilon}$ is greater than a critical nucleation strain ε_c, as follows

$$\widetilde{\varepsilon} = \left\| \langle \varepsilon \rangle \right\|_2^2 \geq \varepsilon_c \tag{4}$$

where ε is the strain tensor and $\widetilde{\varepsilon}$ is the norm of the positive strain tensor (Saceanu et al. 2022). Each nucleation site is then assigned an exclusion radius, so that multiple fractures are not inserted upon one another.

The fractures are inserted at each site as circular discs, comprised of a number of fracture tips. These tips act as the mechanical sources of fracture growth. In the practical modelling of the system, however, there is a limitation on the number of fractures that may be nucleated, so that the number of fracture nuclei does not become computationally unfeasible (see Fig. 2). Consequently, after the calculation of $\widetilde{\varepsilon}$ at all potential sites, the fractures are nucleated at sites of descending $\widetilde{\varepsilon}$, starting with the largest value, if there are more sites fulfilling the $\widetilde{\varepsilon} \geq \varepsilon_c$ criterion than are permitted by the maximum fracture nucleation parameter. This is to prevent any bias introduced by the order in which the sites are inspected.

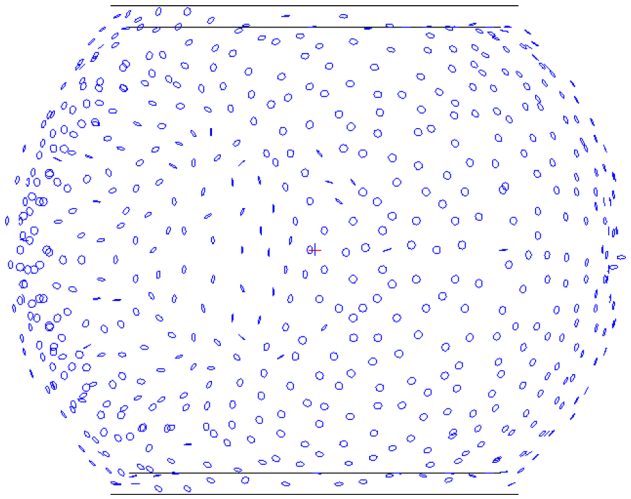


Fig. 2 One hemisphere of the result of an unrestricted nucleation run, yielding 1198 individual fractures shown in blue. The longer of the two horizontal lines at the top (North) and bottom (South) of the figure are 2000 km long. As the domain being modelled is a 1:1 representation of Europa, the outer radius of the domain is 1.56×10^3 km (Color figure online)

2.2.3 Fracture Growth

Fracture growth in the simulator, assuming a quasi-static regime, is governed by the three Stress Intensity Factors (SIFs) for opening, in-plane, and out-of-plane deformation (K_{I}, K_{II}, and K_{III} respectively). Each SIF is calculated for each fracture tip in accordance to the displacement correlation method (Nejati et al. 2015). The computed SIFs are then used to determine whether or not a given fracture tip will grow, and if so, the extent of the growth (Paluszny and Zimmerman 2013).

The determination of whether the tip will extend is drawn from the criterion developed by Richard et al. (2014). This is a mixed-mode propagation criterion that compares the evaluated SIFs to the critical stress intensity factor, K_{IC}, at each fracture tip, as follows

$$\frac{K_{\mathrm{I}}}{2} + \frac{1}{2}\sqrt{K_{\mathrm{I}}^2 + 4(\alpha_1 K_{\mathrm{II}})^2 + 4(\alpha_2 K_{\mathrm{III}})^2} \geq K_{\mathrm{IC}} \tag{5}$$

where α_1 is the ratio of mode I (opening) fracture toughness to mode II (in-plane shear), and α_2 the ratio of mode I toughness to mode III (out-of-plane shear) toughness.

The degree and direction of crack extension are then computed for tips that fulfil the propagation criterion. The extension criterion used in this work (Thomas et al. 2020) is a two-step Paris-type (Paris and Erdogan 1963) law, in which the extension magnitude is dependent on the strain energy release rate at the tip, $\mathcal{G}$, the original radius of a given fracture, Δa_{v}, and two empirical parameters,

β_f and β_n. The energy release rate $\mathcal{G}$ is calculated using an I-integral as described by Nejati et al. (2015), Δa_{v} is a known quantity, and β_f and β_n are assigned standard values (see Table 1). The first step is to calculate the maximum allowed extension, as follows

$$\Delta a_f = \Delta a_{\mathrm{v}} \left(\frac{\mathcal{G}_f}{\mathcal{G}_{\mathrm{v}}} \right)^{\beta_f} \tag{6}$$

where Δa_f is the maximum extension allowed for any tip comprising a fracture, and $\mathcal{G}_f$ and $\mathcal{G}_{\mathrm{v}}$ are the highest value of $\mathcal{G}$ of any tip in the fracture, and the highest value of $\mathcal{G}$ in the whole volume, respectively. The extension for an individual fracture tip, Δa_n, is given by

$$\Delta a_n = \Delta a_f \left(\frac{\mathcal{G}_n}{\mathcal{G}_f} \right)^{\beta_n} \tag{7}$$

where $\mathcal{G}_n$ is the value of $\mathcal{G}$ at the tip. Each tip that passes the propagation criterion will then extend by Δa_n.

The propagation angle criterion described by Richard et al. (2005) yields two angles to control propagation—the perpendicular and tangent angles to the fracture front. For simplicity, in the present work only the perpendicular angle is used, and is calculated as follows

$$\varphi = \mp \left[A \frac{|K_{\mathrm{II}}|}{K_{\mathrm{I}} + |K_{\mathrm{II}}| + |K_{\mathrm{III}}|} + B \left(\frac{|K_{\mathrm{II}}|}{K_{\mathrm{I}} + |K_{\mathrm{II}}| + |K_{\mathrm{III}}|} \right)^2 \right] \tag{8}$$

where $A = 140°$ and $B = -70°$. Further details on this methodology have been given by Paluszny and Zimmerman (2013) and Thomas et al. (2020).

2.3 Time Progression

To capture both diurnal and NSR effects, uniform time-stepping is insufficient. Therefore, two timesteps are used; a diurnal timestep and an NSR timestep, where these intervals alternate along with model growth steps (which are iterative and do not progress time) as follows. The simulator first calculates the stress field at time zero, and iterates through growth steps until either steady state is achieved, or a prescribed maximum number of steps is reached. The simulation time is then incremented by one diurnal timestep, the stress field recalculated, and the growth steps iterate once more. In simulation runs that do not consider NSR, this is the entire algorithm. When NSR effects (primarily stress field translation) are included, after a defined number of diurnal cycles the simulation time is incremented by an NSR timestep, which is orders of magnitude larger than the diurnal timestep. Details of the involved parameters are shown in Table 4 and a schematic representation is shown in Fig 3. In this manner, millions of years of evolution can be simulated while maintaining a temporal resolution sufficient to capture the changes that occur on an hourly basis.

Fractures are assumed to approach a steady state in the diurnal simulation periods before the stress field translates after an NSR timestep, enabling further evolution in the new stress environment. Fracture evolution as a function of time has not been a focus of this work to date, and so the

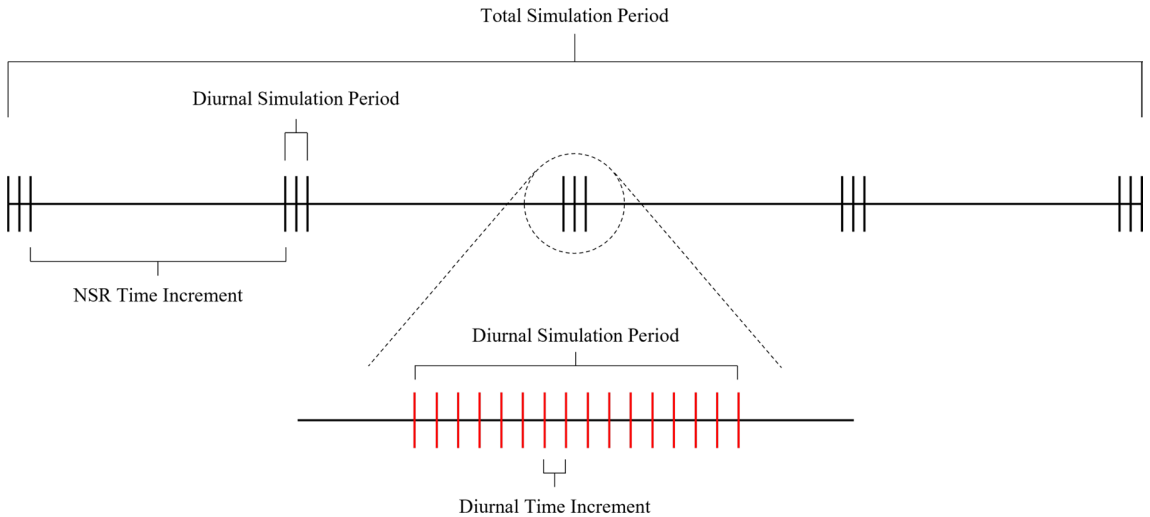


Fig. 3 A not-to-scale schematic representation of the time progression in this simulation. The red lines indicate simulated time steps. In this represented case, there are 4 NSR time increments, which are on the order of 10^5–10^7 years depending on configuration. This leads to five simulated diurnal periods, where each diurnal period consists of 16 modelled increments which have durations of 1–10 h depending on configuration. The number of increments in both cases are low compared to that used in practice and are selected to maintain figure readability (Color figure online)

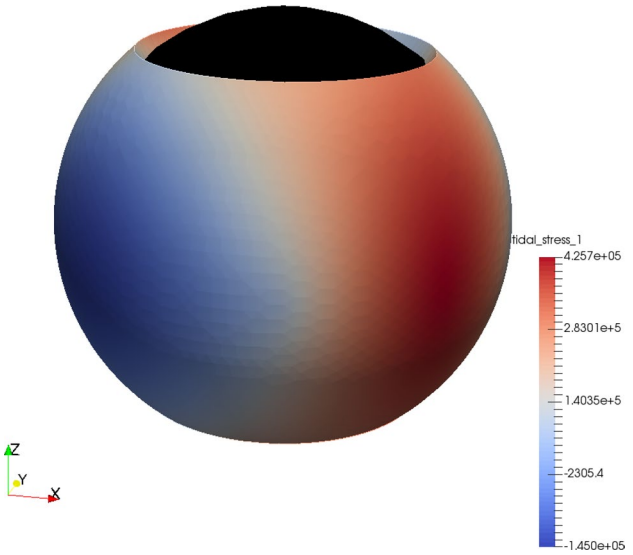


Fig. 4 The modelled domain, where the black sphere represents the silicate core, and the colours give the instantaneous tidal stress across the surface, in this case at periapsis. The radius of the outer sphere is 1.56×10^3 km (Color figure online)

motivator for this time progression scheme was to ensure that both modelled tidal effects, diurnal and NSR, have influence on the results.

3 Simulation Setup

3.1 Simulation Domain

The simulation domain selected for this work consists of the entire surface of Europa, with the inclusion of the subsurface layers (excluding the silicate core), and also excluding 30° cones around the poles (to remove limited numerical artefacting in the polar vicinity). The model domain is shown in Fig 4. To generate the stress field, the tidal stress model described prior is evaluated at every node in the domain.

The outer surface of the ice, and the interior surface, are set as Dirichlet boundaries. The interior faces exposed by the removal of the polar cones are set as symmetric boundaries to minimise their influence. The tidal stresses are applied as volumetric body forces.

3.2 Physical Parameters

The physical quantities that parameterise the system along with their values are detailed in Table 1. The physical parameters for ice on Europa are associated with very low temperatures, and therefore the references given in the table have been obtained from low temperature testing, where possible. The literature for ice at these temperatures is not extensive, however, especially in the Europa context, and so where low temperature experiments are not available, best estimates are used. The parameters

Table 1 Summary of physical parameters

Physical parameter	Symbol	Value	Unit	References
Young's modulus of ice	E	9	GPa	Nimmo (2004)
Fracture toughness of ice	K_{IC}	108	kPa $m^{\frac{1}{2}}$	Goodman (1980)
Poisson's ratio of ice	σ	0.33	–	Sinha (1989)
Tensile strength of ice	UTS	2	MPa	Petrovic (2003)
Diurnal angular rate	f_{diurnal}	2.0485×10^{-5}	rad s^{-1}	Burns et al. (1986)
NSR angular rate	f_{NSR}	1.7434×10^{-14}	rad s^{-1}	Geissler et al. (1998)
Orbital eccentricity	ϵ	0.0094	–	Cassen et al. (1979)
Jovian Mass	M_{Jupiter}	1.898×10^{27}	kg	Jacobson et al. (2000)
Eur. mass	M_{Europa}	4.799×10^{22}	kg	Jacobson et al. (2000)
Eur. radius	R_{Europa}	1.561×10^3	km	Archinal et al. (2018)
Jovian semi-major axis	a_{Jupiter}	7.78479×10^8	km	Office et al. (2016)
Eur. semi-major axis	a_{Europa}	6.71×10^5	km	Cassen et al. (1979)
Eur. surface gravity	g	1.315	m s^{-2}	Derived
Lamé μ	μ	3.487	GPa	Gammon et al. (1983)
Lamé λ	λ	9.3	GPa	Gammon et al. (1983)
Brittle ice viscosity	ν_{Brittle}	1×10^{22}	Pa s	Wahr et al. (2009)
Paris exponent f	β_f	0.35	–	Paris and Erdogan (1963)
Paris exponent n	β_n	1	–	Paris and Erdogan (1963)

of relevance affected by temperature are fracture toughness (Liu and Miller 1979) and ultimate tensile strength (Haynes 1978), although both show only a weak correlation with temperature. The Young's modulus of ice shows a discrepancy between laboratory and field measurement, although in the case of Europa this has been resolved by Nimmo (2004) where the laboratory value is determined to be the superior estimate, also showing low sensitivity to this quantity in the Europa system. The only free parameter is the NSR angular rate, f_{NSR}, as the NSR period is not well constrained; it has a lower bound between 10^4 years (Geissler et al. 1998) and 7×10^5 years (Ashkenazy et al. 2023) and an indeterminate upper bound as very high NSR periods would be undetectable. The angular rate of 1.7434×10^{-14} rad s^{-1} (corresponding to a period of 1.42×10^7 years) has been selected such that the NSR stresses yielded are of the same order as the diurnal stresses. This is so that neither effect will dominate over the other.

3.2.1 Love Numbers

The Love numbers, h, k and l, are complex dimensionless quantities that parameterise the rigidity of a body in response to tidal forcing, where in this work h describes the amplitude of the radial displacement of the Europan surface, l describes the tangential components of the displacement, and k is not used. Details about Love numbers are given by Agnew (2015). The tidal response of the layers not directly considered by the simulator, such as the silicate core, are incorporated into the model through their effect on the Love numbers.

The tidal stress simulator used in this work relies on computed second-degree Love numbers, which are taken from Wahr et al. (2009) and detailed in Table 3 with the necessary parameters in Table 2. The Love numbers are very weakly dependent on the NSR period, and the imaginary component is always substantially smaller than the real component. Therefore, variations in the material properties yield no significant change in these quantities; see Wahr et al. (2009) for further detail. With regard to the present work, any changes that would arise in the Love numbers due to alteration of the model are not considered due to the insignificant magnitude of the differences that would ensue.

Table 2 Summary of parameters pertinent to Love numbers, taken from Wahr et al. (2009)

Physical parameter	Symbol	Value	Unit
Mean density of Europa	ρ_{Europa}	3012.6	kg m^{-3}
Young's modulus of rock	E_{Rock}	100	GPa
Poisson's ratio of rock	σ_{Rock}	0.25	–
Mean density of ice	ρ_{Ice}	940.0	kg m^{-3}
Mean density of rock	ρ_{Rock}	3847.6	kg m^{-3}
Density of water	ρ_{Ocean}	1000.0	kg m^{-3}
Ductile ice viscosity	η_{Ductile}	1×10^{17}	Pa s
Fluid P-wave velocity	v_P^{Ocean}	1.45	km s^{-1}
Brittle ice P-wave velocity	v_P^{Brittle}	3.466	km s^{-1}
Brittle ice S-wave velocity	v_S^{Brittle}	1.839	km s^{-1}

Table 3 Model Love numbers, taken from Wahr et al. (2009)

Love number	Symbol	Real component	Imaginary component
Diurnal love number h	h_{diurnal}	1.192	-6.293×10^{-5}
NSR love number h	h_{NSR}	1.813	-4.186×10^{-3}
Diurnal love number l	l_{diurnal}	0.3094	-2.903×10^{-5}
NSR love number l	l_{NSR}	0.4748	-2.766×10^{-3}

3.3 Geometric and Model Parameters

The domain of Europa is defined using a boundary representation of three dimensional non-uniform rational b-splines. The spline object is then meshed volumetrically with an octree method, using isoparameteric tetrahedra and triangles. The resultant mesh is at 1:1 scale to Europa. The meshes begin with approximately 70,000 nodes and 50,000 elements, which climbs to a maximum of approximately 600,000–800,000 nodes and elements as the simulation develops. The simulations presented in this work were run on a 44-core Intel Xeon Gold 6238 CPU at 2.10 GHz, with 64 GB of system memory. The simulations take between one to three days to execute.

3.3.1 Layering

The simulations executed in this work primarily fall under two configurations, the layered and non-layered cases. In the simpler non-layered case, the silicate core is encased in a thick brittle ice layer and nothing else, as a control for a Europa without a contiguous oceanic layer and weaker tidal heating effect. In this case the ice is modelled as being 140 km thick, assuming the absence of an oceanic layer. This brittle ice uses the values listed in Table 1.

The other case is that of the layered moon, incorporating both the oceanic layer and ice layer, in which the ice layer is subdivided into a deeper, warmer, ductile layer, and an outer, colder, brittle layer. The thickness of the simulation domain is forced to be larger than the physical situation due to modelling constraints on thin domains. In reality, the ice crust is believed to be a maximum of 2%

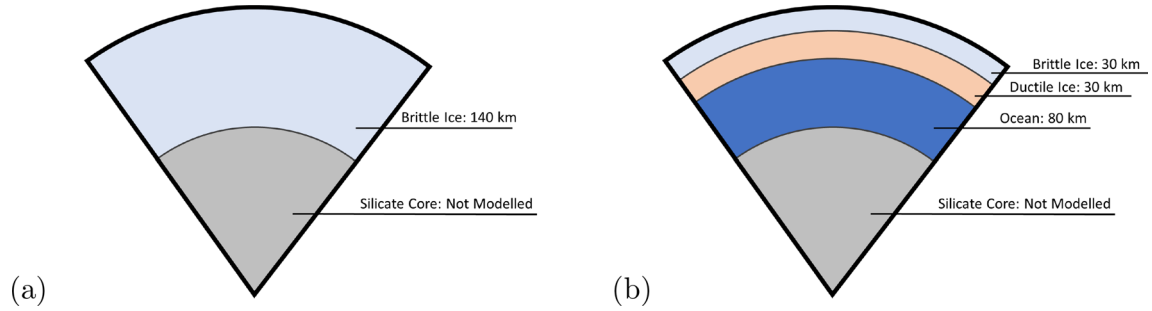


Fig. 5 Schematic representations of the two layering cases for comparison. Not to scale. **a** Shows the single layered configuration. Radius of the wedge is 1560 km. **b** Shows the three layered configuration. Radius of the wedge is 1560 km

(assuming the maximum estimate of 30 km) of the total body radius, which is presently unfeasibly thin for the numerical model and computational time constraints. To counteract this the thickness of the ice layer is increased from an estimated 20–60 km and the oceanic layer reduced to 80 km from 100 km. It is not well understood where the division from ductile to brittle ice lies, nor how sharp or blurred the boundary may be, therefore as a first-line assumption the ductile and brittle ice layers are both taken to be half of the overall ice thickness. Thus the layers in the three layer case are organised as follows: 80 km thick ocean, 30 km thick ductile ice and 30 km thick brittle ice (see Fig. 5).

Although the simulation domain is dimensionally inaccurate to the most attested values, the stress calculation is wholly derived from the most well-understood physical parameters, with only the simulation domain being altered and therefore the effect on the results is expected to be minimal.

In the layered case, the oceanic layer is modelled as a soft body that is unable to fracture. The ductile layer is modelled with the same physical parameters as the brittle layer at the interface between the two layers, and the physical parameters are set to those of ice at 0 °C at the ice-ocean interface, with the values changing monotonically with depth between the two interfaces.

3.3.2 Melt-Water Lenses

Another tested scenario is the presence of subsurface melt-water lenses (Vilella et al. 2020). These lenses have been theorised to be the motivating phenomena behind the formation of chaos terrain, and possibly also the lenticulae, on the Europan surface (Schmidt et al. 2011), by inducing increased fracturing in the region between the lens and the surface, and thus allowing liquid water from the lens to float "rafts" on the surface creating these features once refrozen.

The lenses are modelled in this work as spherical regions of heterogeneity in the brittle ice, wherein 16 such regions are distributed randomly throughout the brittle layer. The material properties of the ice within these regions are changed to that of the oceanic layer, to model the liquid water present within the lens. The diameters of the regions are randomly assigned between 5 and 80 km, using the observed sizes of lenticulae and chaos as a guide (Schmidt et al. 2011; Culha and Manga 2016).

3.3.3 Parameter Summary

The model parameters are summarised in Table 4. The maximum growth steps parameter, n_{Growth}, controls how many times fractures may extend within a given diurnal timestep. The maximum step extension, e_{Step}, is a multiplier on the initial fracture radius to control the maximum extension allowed in a given growth step (i.e. with the given values for initial fracture radius and maximum step extension of 10 and 2 km respectively, the maximum distance a fracture tip may extend is 20 km, even if the result returned by Eq. 5 is larger). The mid-step and NSR step nucleation parameters, N_{Step} and N_{NSR}, denote the number of new additional fractures allowed to nucleate in the middle of an NSR timestep and at the end of an NSR timestep, respectively.

4 Results and Discussion

The results of simulations conducted with a single layer and three layers are shown in Figs. 6 and 7, respectively. Both simulations operate under the diurnal regime, excluding the NSR stress field translation. The initial nucleation number was 20, with an additional twenty nucleations added after every eight diurnal time steps. In the three-layer scenario, the ocean has a thickness of 80 km, followed by a 30 km thick ductile layer, and topped with a 30 km thick brittle layer. Both cases undergo the nucleation of 60 fractures over the course of the simulation run. For the cases with limited

Table 4 Summary of model parameters

	Model parameter	Symbol	Value	Unit
Time and growth	Diurnal cycle period	T_{diurnal}	3.06822×10^5	s
	Diurnal timestep	t_{diurnal}	3.83528×10^4	s
	NSR cycle period	T_{NSR}	3.15576×10^{14}	s
	NSR timestep	t_{NSR}	3.94470×10^{13}	s
	Maximum growth steps	n_{Growth}	5	1
Fracture parameters	Initial fractures	$N_{\text{Fractures}}$	80	1
	Fracture initial radius	$r_{\text{Fractures}}$	10	km
	Fracture spacing	$\delta_{\text{Fractures}}$	10	km
	Maximum step extension	e_{Step}	2	1
	Mid-step nucleation	N_{Step}	5	1
	NSR step nucleation	N_{NSR}	80	1
Ductile layer	Outer radius of domain	$R_{\text{Outer}}^{\text{Ductile}}$	1530	km
	Inner radius of domain	$R_{\text{Inner}}^{\text{Ductile}}$	1500	km
Oceanic layer	Outer radius of domain	$R_{\text{Outer}}^{\text{Oceanic}}$	1500	km
	Inner radius of domain	$R_{\text{Inner}}^{\text{Oceanic}}$	1420	km
Meltwater lenses	Number	N^{Lenses}	16	1
	Radius	r_{Lenses}	5–80	km
	Depth	d_{Lenses}	4–20	km

nucleation sites, as these, fractures are nucleated first in regions where most damage is present, so as to capture the progression of damage in the most relevant locations first, before re-evaluating stresses.

Figures 6a, 7a, as well as 6b, 7b show a view of the entire simulation domain from the y-axis and z-axis, respectively, offering an overview of the entire fracture pattern. Notably, fractures nucleate in two distinct, nearly symmetric clusters, directly corresponding to the most tensile regions depicted in Fig. 1. These patterns are likely to repeat a stagger as a function of time, with subsequent effects of healing and interaction which are not taken into account in the present models. The resulting fracture patterns exhibit similarities, although the three-layer case reveals some nucleation occurring outside of the main clusters and within the compressive region, as highlighted by the red circles in Fig. 7b. This is hypothesised to be a result of the layering within the domain, which intensifies stress concentrations, thereby promoting additional nucleation at these sites. Figures 6c and 7c provide a closer examination of the respective primary fracture clusters. Both reveal a shared overall structure—a distinct North–South aligned feature to the East of the cluster and a curved feature to the West. The East–West fracture asymmetry is explained by the diurnal asymmetric behaviour depicted in Fig. 8, where (a) illustrates the most East-leaning stress field, and 8b shows the most West-leaning. The stress magnitude of the East-leaning state is significantly larger, thus exerting dominance over the fracture growth behaviour throughout the growth cycle, resulting in the fracture clusters adopting its characteristic form.

When comparing Fig. 7c, to Fig. 6c, a qualitative difference is the relative lack of growth of the smaller fractures beyond the major observed features. This suggests that in the three-layer case, a greater amount of stress is dissipated through deformation in the dominant fractured regions, resulting in lesser-magnitude stress intensity factors (SIFs) for the remaining network. Figures 6d, e and 7d, e are views of a selected representative primary feature fracture. The (d) subfigures provide a profile view from East to West, where the cyan surface represents the silicate core boundary. The (e) subfigures offer a plan view looking down to the surface. The plan views exhibit a similar form, with minimal deflection from the initial fracture plane, attributable to the absence of rapid spatial changes in the stress field, allowing predominantly linear extension.

In contrast, the profile perspectives reveal a contrast in terms of the existence of multiple layers. Figure 6d depicts the ovoid shape of fractures in the unlayered case, which extend through the entire crust to the silicate core. This aligns with the anticipated outcome when modelling a fracture in a weakly spatially-varying stress field. On the other hand, Fig. 7d takes on a different configuration—the fracture does not breach the oceanic layer. Instead, it assumes a crescent shape, with the leading edges of the fracture being deflected away from the oceanic layer. This phenomenon may be attributed to the less favourable conditions for fracture growth in the ductile ice compared to the brittle ice layer.

Figure 9 illustrates the outcomes of a single-layer simulation under an NSR regime, conducted for approximately 10^8 Earth years. The mechanical properties employed are

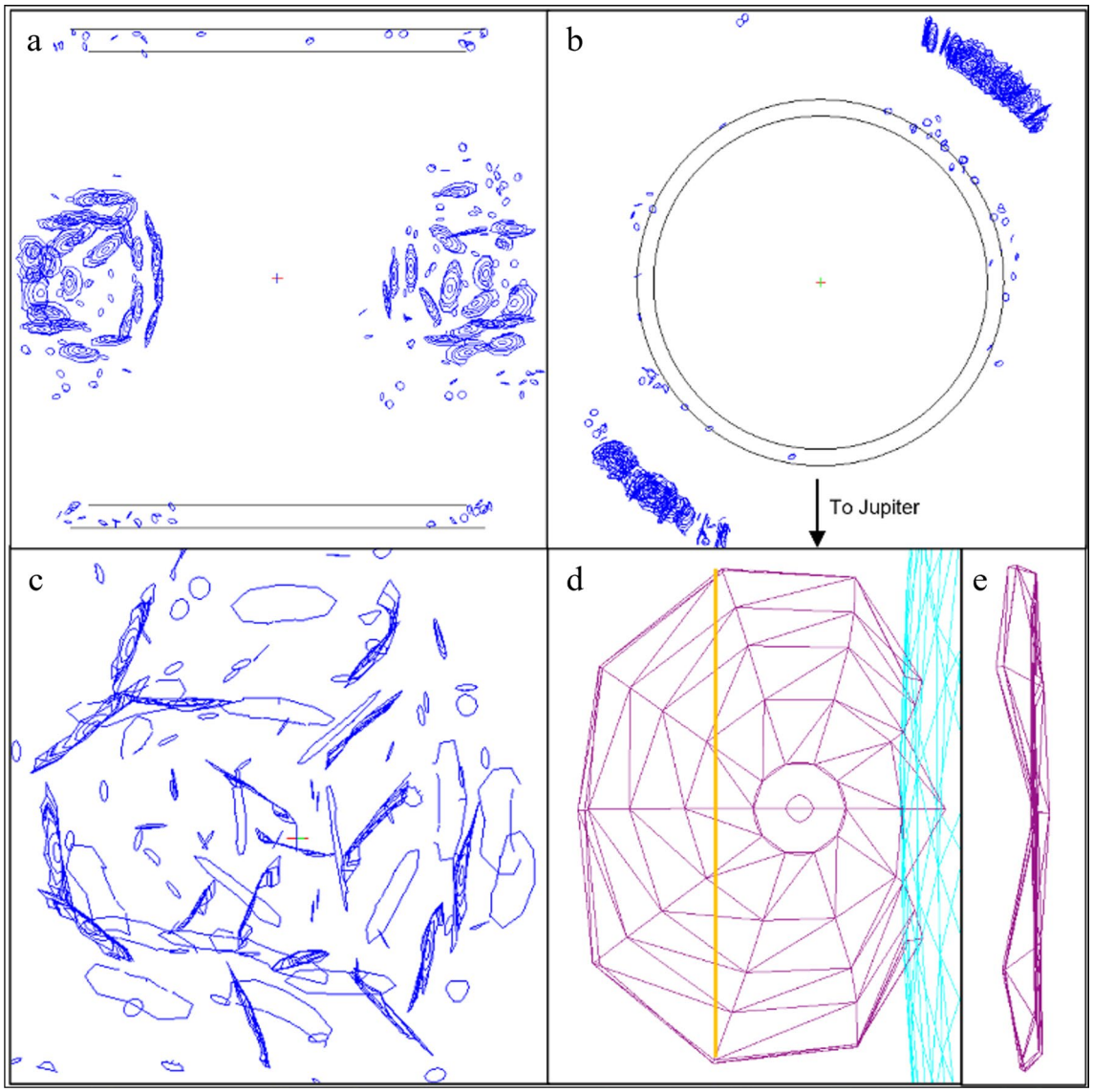


Fig. 6 Single layer growth for a diurnal regime. **a** The *y*-axis or equatorial view. The longer of the two horizontal lines at the top and bottom of the figure are 2000 km long. **b** The *z*-axis or polar view. The outer black circle has a diameter of 2000 km. **c** A detail of one primary fracture cluster. **d** A detail of the profile of one representative fracture. The cyan denotes the silicate core boundary and the orange denotes the longest span of 212 km. **e** Shows the plan view of the same fracture (Color figure online)

consistent with the previous single-layer case. Throughout the simulation, a total of eighty fractures are nucleated, including several smaller nucleations during the mid-diurnal phase.

Figure 9a shows minimal deviation from Figs. 6, 7a, aside from a reduction in out-of-cluster nucleations. In Fig. 9b, the effect of the NSR regime becomes evident, revealing three distinct pairs of fracture clusters. The relative formation periods of the clusters are distinguishable by observing the comparative development of the primary fractures in each cluster, where the most developed cluster is usually the first to have formed (see Fig. 9c). This suggests that, although the highest stresses for fracture nucleation are concentrated in the tensile region, which hosts the fracture clusters, there are still sufficiently strong tides present in other parts of the crust to drive additional fracture growth away from these

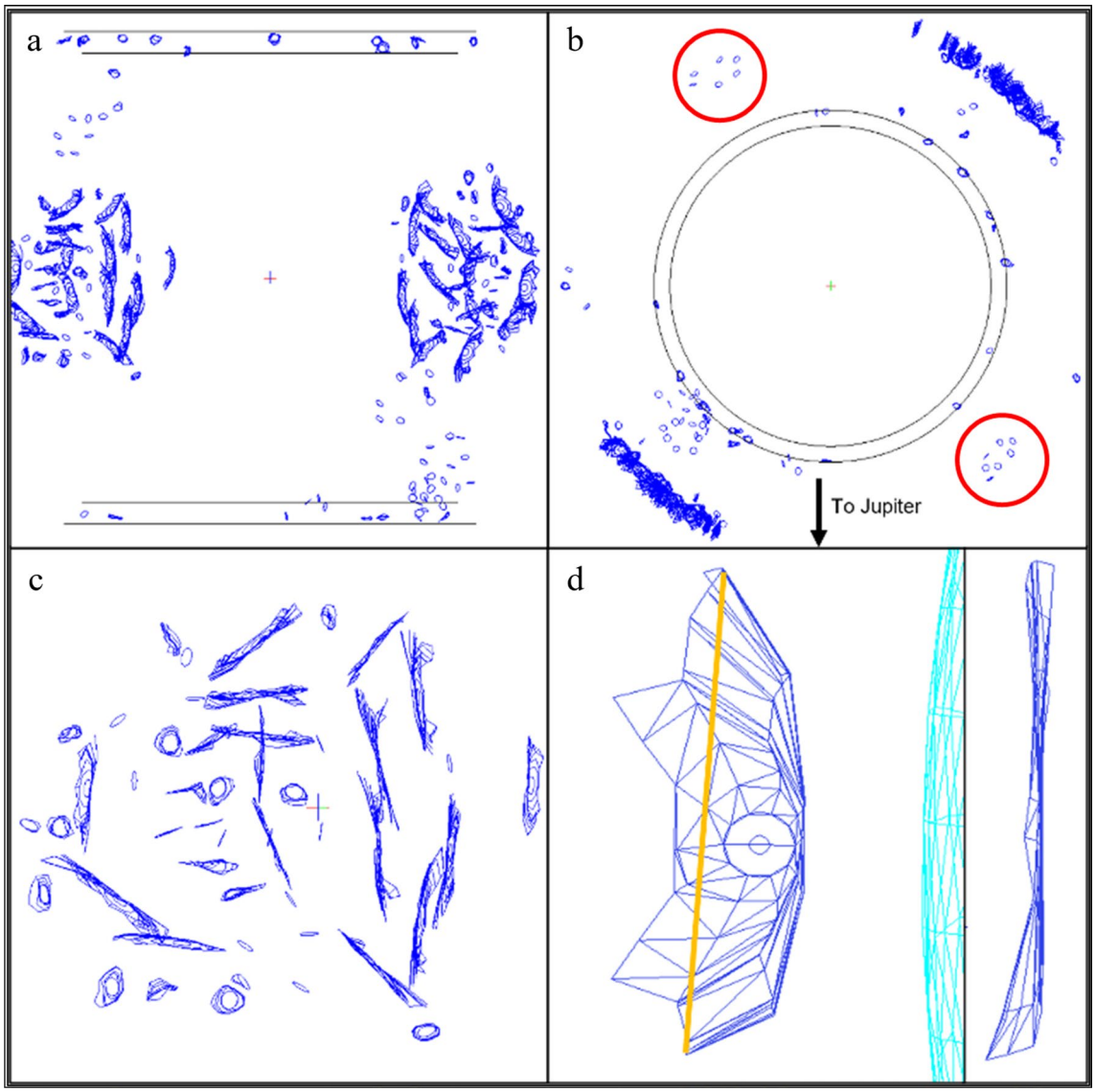


Fig. 7 Three-layer growth for a diurnal regime. **a** The *y*-axis or equatorial view. The longer of the two horizontal lines at the top and bottom of the figure are 2000 km long. **b** The *z*-axis or polar view. Red circles denote fracture nucleation outside the primary clusters. The outer black circle has a diameter of 2000 km. **c** Detail of one primary fracture cluster. **d** Detail of the profile of one representative fracture. The cyan denotes the silicate core boundary and the orange denotes the longest span of 292 km. The 'spikes' are numerical artefacts. **e** Plan view of the same fracture (Color figure online)

regions. Notice that the secondary fracture cluster seen in Fig. 9d is also significantly more diffuse and less developed than the primary cluster in Fig. 9c. This underlying mechanism that drives increased separation in the later nucleation sites is probably related to the local release of stresses within the more developed clusters.

The simulation depicted in Fig. 9 is quantified in Fig. 10 using P metrics that have been slightly modified (Pierce 2017). In this scheme, P*ij* represents a metric in which *i* denotes the dimension of the sample domain, and *j* signifies the dimension of the sampled quantity. For instance, P32 quantifies the area of fractures in the domain per unit volume. In this study, the P20, P21, P30, and P32 metrics

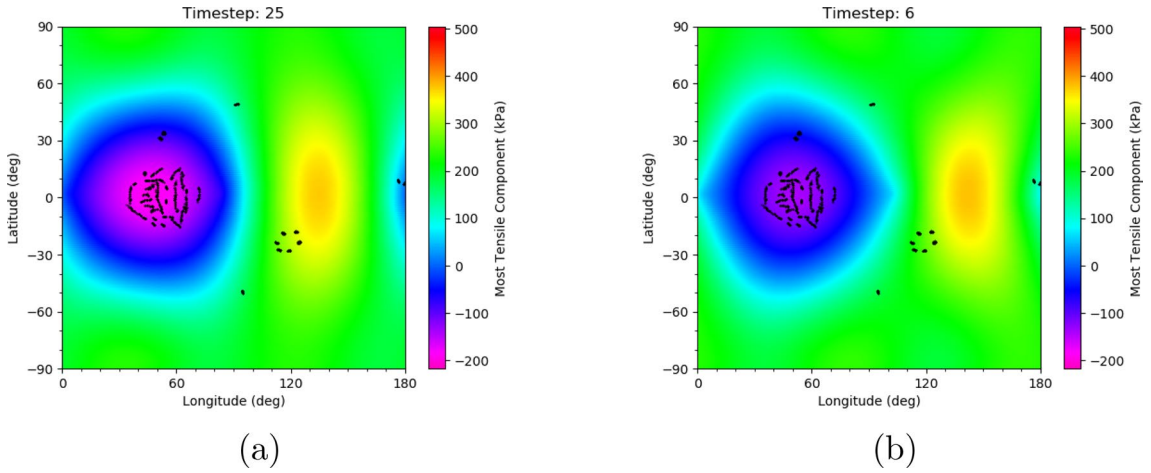


Fig. 8 Differing times in the diurnal stress field with the final state of the associated surface-intersecting fracture patterns to show how the pattern matches the stress field. **a** Shows the most Easterly lean of the tensile region, where one can see how the right-hand of the pattern aligns with the stress field. **b** The corresponding Westerly lean, where one can see how the left-hand of the patterns aligns with the stress field

are employed (Dershowitz et al. 2020). Notably, the P20 and P21 metrics are modified to specifically account for the amount (P20) and length (P21) of intersections of fractures with the external surface of the ice, representing the theoretically visible portion of the fractures. This stems from the fact that the sole observational data available for Europa concerning fracturing and lineae are mission images capturing the surface. Therefore, these images constitute the only elements in this study directly connected to observations.

The P20 metric, plotted in Fig. 10a, initiates from 0, indicating that no fractures are permitted to nucleate in contact with any boundary. P20 then increases in a stepwise manner thereafter. This suggests that the fractures in growth progress at a closely matched rate, resulting in their simultaneous intersection with the boundary. This pattern is observed again in Fig. 10b, where the P21 metric is plotted, with a slight later evolution as compared to the progression of amount of fractures generated (P20). Figure 10a, b demonstrate that subsequent nucleations have a less significant impact on the surface compared to the initial fracture cluster, and that the pattern is dominated by the rapid growth of initially nucleated fractures.

The steep rises seen in the P30 metric (Fig. 10c) correspond to the major nucleation events that occur at the NSR time scale, with the lesser steps corresponding to nucleations during the mid-diurnal-cycle. Figure 10d plots the evolution of the P32 fracture surface intensity metric, revealing a gradual yet steady increase in fracture area, which stands in contrast to the sharp ascent observed in the P20 and P21 metrics, corresponding to fracture amount and fracture line intersections with the surface. This can be attributed to the fact that subsurface behaviour remains largely unaffected by surface interaction, allowing fractures to persist in their growth even when the rate of surface intersection growth has decelerated. The P32 metric encompasses fractures that have not breached the surface, which grow under the surface without having a surface footprint. However, as previously discussed, primary fractures typically exhibit concurrent growth, resulting in relatively inactive fractures remaining entirely within the subsurface.

Results from a simulation featuring inserted meltwater lens heterogeneities are presented in Fig. 11. In Fig. 11a, a primary fracture cluster is depicted, resembling those previously discussed. However, some fractures have nucleated in the vicinity of a subsurface lens. Figure 11b displays a 'standard' vertically orientated fracture, similar to those observed in the preceding three-layer models. Notably, Fig. 11c showcases a fracture proximate to the lens with a horizontal orientation, a characteristic that is not observed in the absence of the lens. Figure 11d shows that despite the original fracture nucleus being inserted with an initially semi-vertical alignment, commonly observed in other results, the fracture rapidly grows changing its orientation to become parallel with the ice surface, above the lens. This phenomenon suggests that the horizontal fractures, when

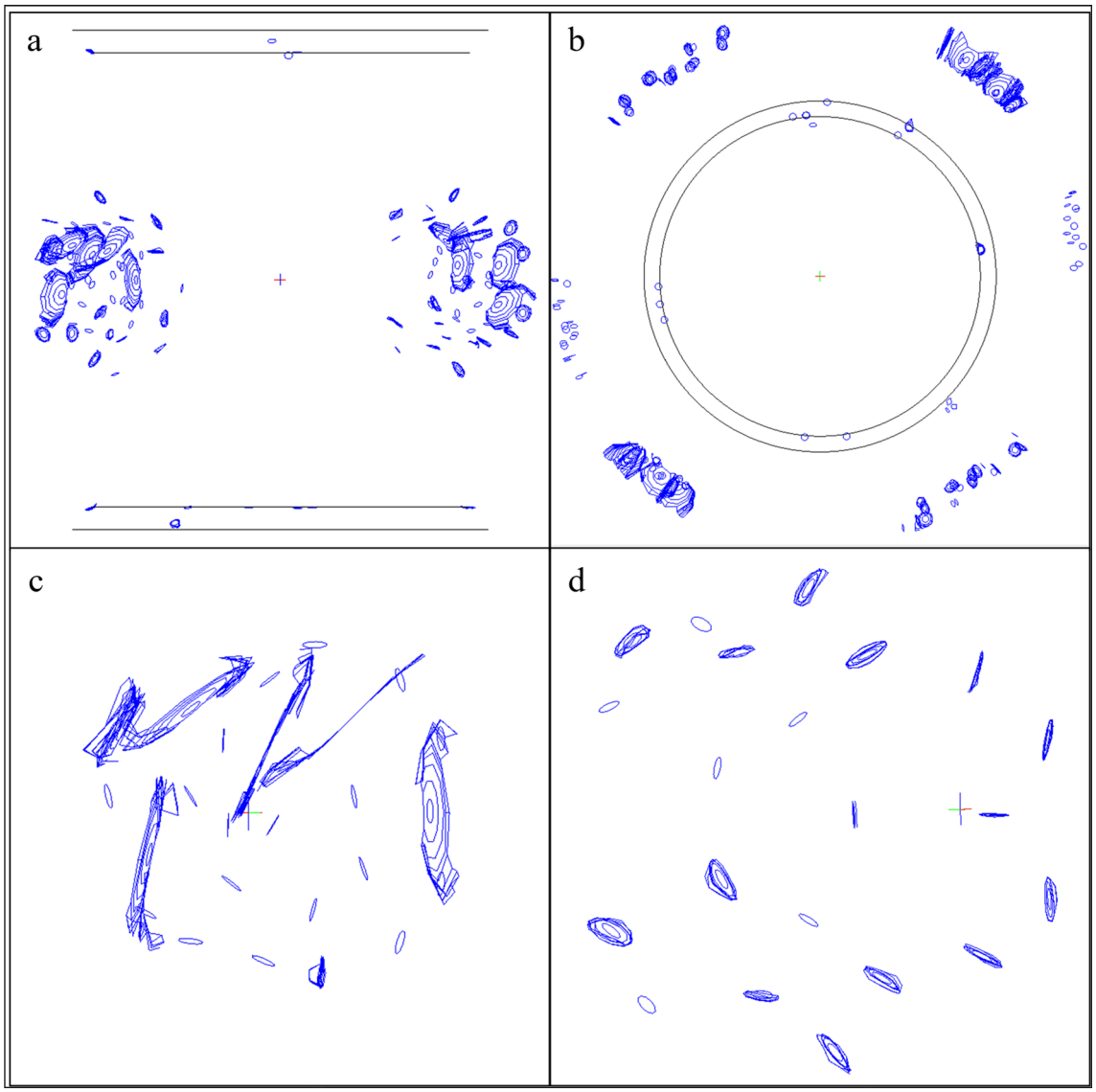


Fig. 9 Single layer growth for an NSR regime. **a** Gives the *y*-axis or equatorial view. The longer of the two horizontal lines at the top and bottom of the figure are 2000 km long. **b** Gives the *z*-axis or polar view. The outer black circle has a diameter of 2000 km. **c** Shows one of the two primary (first to nucleate) fracture clusters. **d** Shows one of the secondary fracture clusters

parallel and in proximity to the surface, may weaken and disrupt the surface, potentially contributing to the formation of the observed chaos or lenticulae features.

Figure 12 shows a number of simulation runs with varying conditions of NSR, layering, heterogeneities, and temporal resolution, amongst other quantities. Together, these illustrate how the combination of the modelled physical processes can produce a more complete model of how the Europan surface may develop as a function of time. In Fig. 12a, b, the smaller discs are fractures that nucleated but their growth did not progress thereafter. In the depicted cases the only nucleation limit applied in a minimum spacing at the nucleation time, so that no further fracture is nucleated in the vicinity of a recently nucleated fracture location without recalculating the stress field (as the new fracture is likely to have affected the stress distribution at the nucleated site).

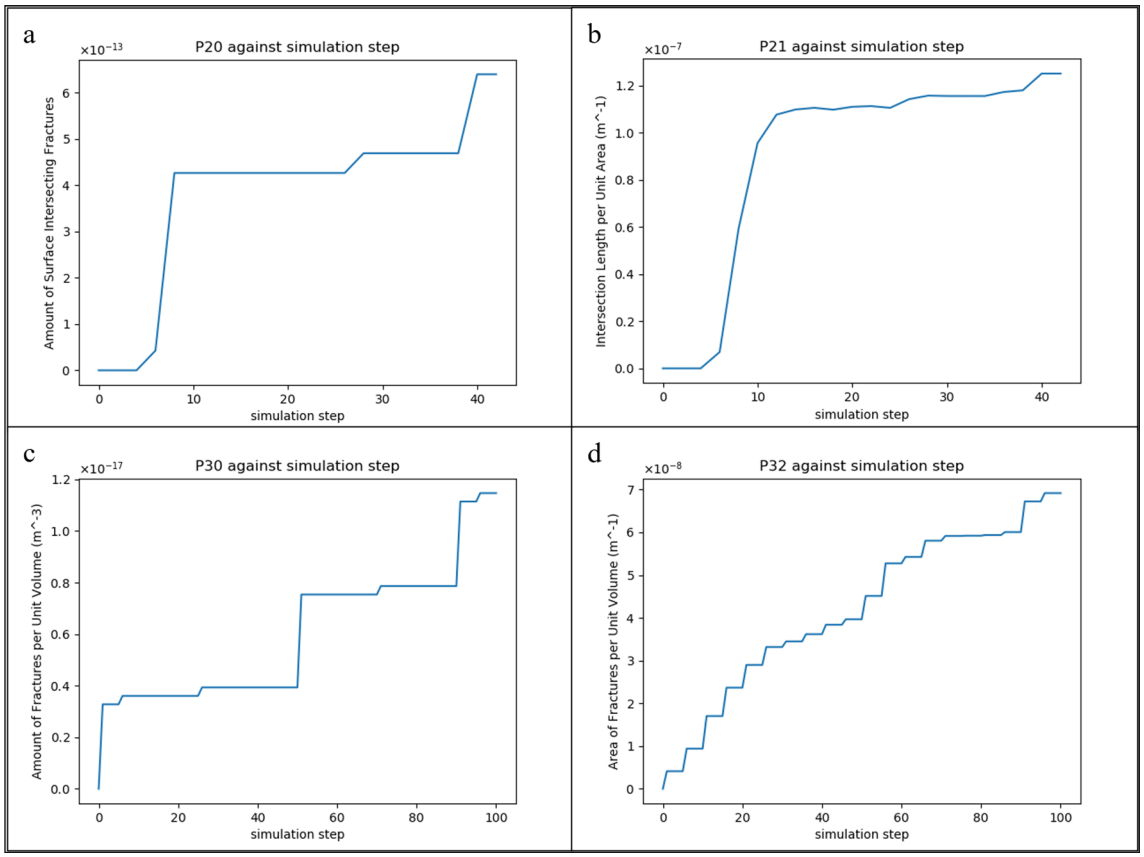


Fig. 10 Fracture intensities for the simulation shown in Fig. 9. **a** A modified P20 metric to only consider the number of fractures that intersect the outer surface against simulation step. **b** A modified P21 metric to only consider the length of fracture intersection with the outer surface of the ice against simulation step. **c** The P30 metric against simulation step. **d** The P32 metric against simulation step

This lax constraint leads to a substantially higher number of fractures being nucleated, in this case yielding 1198 separate fracture nuclei. These findings suggest that the majority of the surface experiences significant stress, leading to periodic fracture nucleation.

Figure 12d shows only traces of fractures that intersect the surface of Europa, which would have a visible footprint on the surface. Figure 12e shows the same, but also including the 3D shape of the fracture surface at depth. Figure 12d, e show an individual fracture cluster, a group of larger fractures that concentrates to form these structured patterns. Clusters can be qualitatively compared to images of the Europan surface, taken by the Galileo mission (see Fig. 12c, f). Both patterns displays similar characteristics of fracture cross-cutting and clustering, in particular regarding the North–South oriented features interspersed with weaker East–West features, collectively surrounded, by a number of smaller fractures with disparate orientations.

5 Concluding Remarks

The growth of fracture networks on the Europan surface has been investigated using a finite element fracture simulator, to qualitatively determine whether the behaviour of the large-scale lineae observed on the surface can be modelled by linear elastic fracture mechanics. The preliminary set of fracture patterns appears to show consistency with observations of Europan lineae. Fractures distribute in particular around the equatorial region, and self-organise to form networks that qualitatively resemble some of the features observed on the surface of Europa. Interesting behaviour in the unobserved subsurface is also simulated,

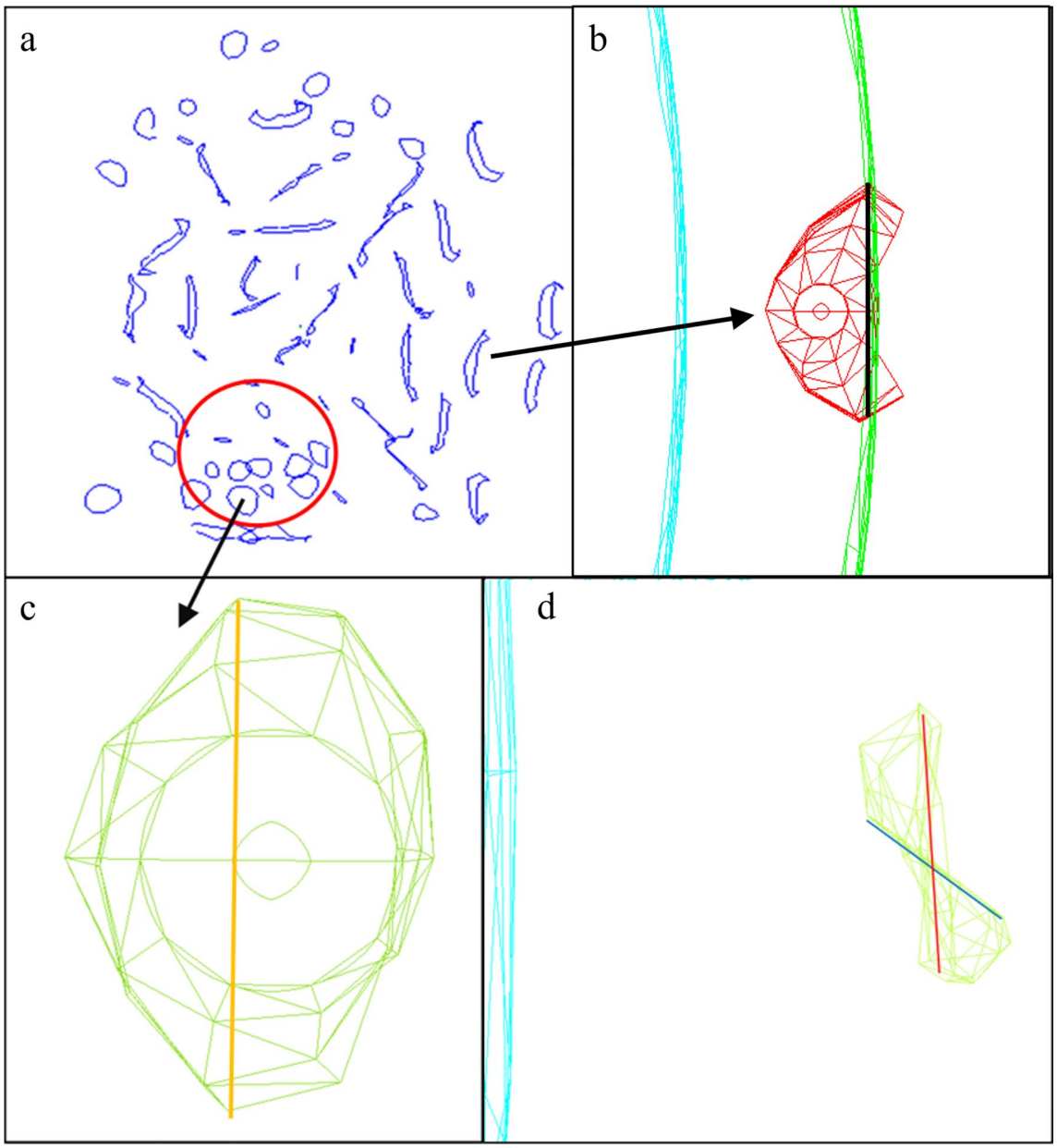


Fig. 11 A three-layered diurnal regime simulation, with melt-water lenses inserted into the ice. **a** A primary fracture cluster. The red circle denotes the approximate location of an inserted subsurface melt-water lens. Notice the upturned fractures in the vicinity of the lens. **b** Profile of a representative fracture, indicated by an arrow. The fracture length as shown in black is 170 km. The blue denotes the silicate layer boundary, and the green denotes the outer surface of Europa. **c** The profile of an upturned fracture, indicated by an arrow. Fracture length as shown in orange is 79 km. **d** An alternate view of the fracture in **c**, parallel to the surface. Notice the pronounced deflection (shown by the red line) of the original fracture nucleus (denoted by the blue line) to align with the silicate layer (denoted by the cyan mesh) and therefore also align with the surface. Further notice the divergence between the standard, representative fracture shown in **b** and the surface parallel fracture in **c**, **d**, underlining the speciation of the upturned, surface-parallel fractures (Color figure online)

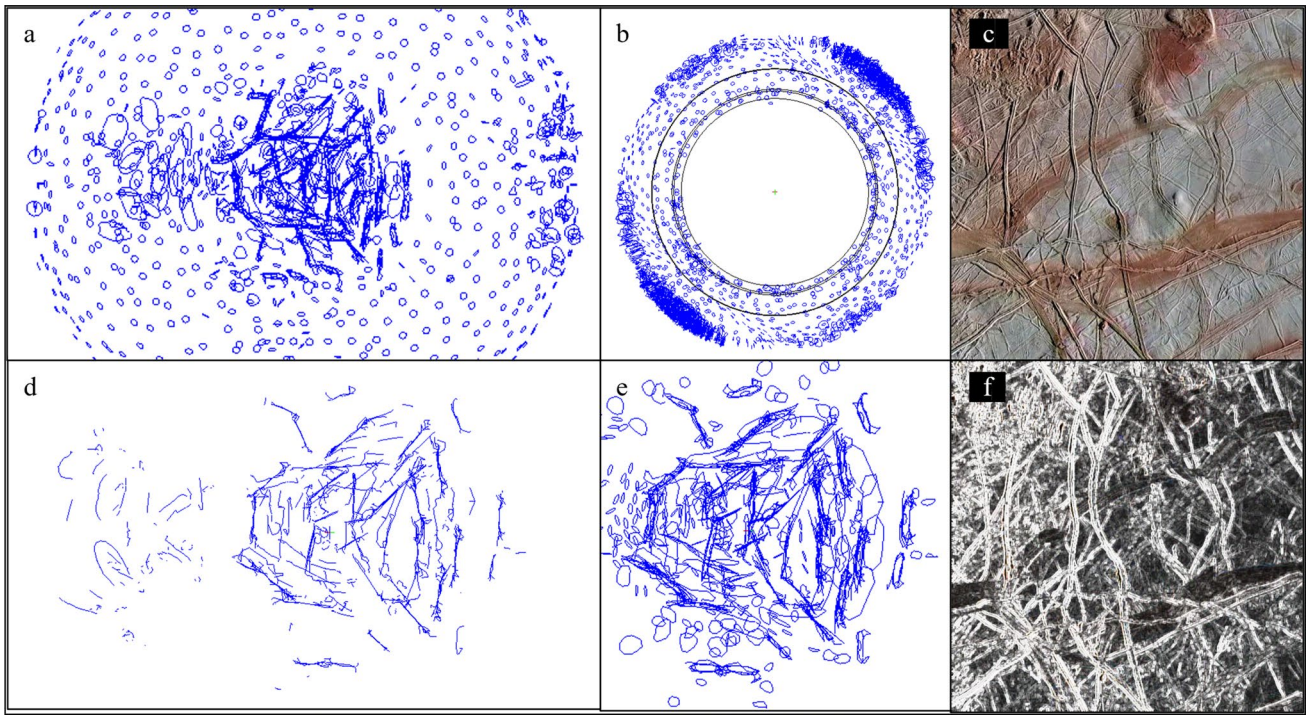


Fig. 12 A consolidation of multiple simulations into one domain. **a** A primary fracture cluster. The many smaller fractures are the result of a nucleation without a quantity cap. **b** The *z*-axis or polar view. The outer black circle has a diameter of 2000 km. **c** A representative region of the Europan surface, approximately 230 km square, Image Credit: NASA JPL. **d** The same fracture cluster as **a** but only showing surface intersecting traces. **e** The same fracture cluster as **a**, but only showing surface intersecting fractures. **f** The same region imaged in **c** with an edge detection filter to better emphasise the lineae, again approximately 230 km square

especially with regards to meltwater lenses and their effect upon surface features. In the vicinity of these lenses fractures are observed to adopt a horizontal orientation parallel to the surface, providing a potential rationale for the development of chaos regions in the weakened zones formed above lenses. These findings serve as a proof of concept of this modelling approach in this context and are the basis for ongoing work into lineae behaviour on the Europan surface. In the context of fracture mechanics, this application presents a challenging high-density fracture growth scenario, in a layered medium subjected to constant in situ stress variations. As opposed to traditional simulations, the scale and magnitude of spatially and temporally varying stresses requires constant re-evaluation of the nucleation and growth of fractures in the domain. Further work requires investigation into the effects of layering, material property definition, heterogeneities, fracture healing, and the representation of denser fracture systems. This approach is also particularly well-disposed to studying the effect of strike-slip along lineae and the possible consequences of this for resurfacing.

Acknowledgements The authors thank the Royal Society for funding this research through fellowship URF\R\221050, and award RGF\R1\181016. The authors also thank NASA for access to observational data of Europa.

Author Contributions Study conception and design was performed by AP and JW. Acquisition of the financial support for the project leading to this publication was performed by AP. Oversight and leadership responsibility for the research activity planning and execution was performed by AP and RZ. The original ICGT code was written by AP. The ICGT code was modified to the specific problem and the tidal stress model was updated to C++ by JW. Numerical model setup, design and analysis and visualisation was performed by JW. The first draft of the manuscript was written by JW and all authors commented on previous versions of the manuscript. All authors read, edited and approved the final manuscript.

Funding This work was funded by the Royal Society through fellowship URF\R\221050 and award RGF\R1\181016.

Data availability Not applicable.

Declarations

Conflict of interest The authors have no conflict of interest.

Open Access This article is licensed under a Creative Commons Attribution 4.0 International License, which permits use, sharing, adaptation, distribution and reproduction in any medium or format, as long as you give appropriate credit to the original author(s) and the source, provide a link to the Creative Commons licence, and indicate if changes were made. The images or other third party material in this article are included in the article's Creative Commons licence, unless indicated otherwise in a credit line to the material. If material is not included in the article's Creative Commons licence and your intended use is not permitted by statutory regulation or exceeds the permitted use, you will need to obtain permission directly from the copyright holder. To view a copy of this licence, visit http://creativecommons.org/licenses/by/4.0/.

References

Agnew D (2015) 3.06—Earth tides. In: Schubert G (ed) Treatise on geophysics, 2nd edn. Elsevier, Oxford, pp 151–178

Archinal B, Acton C, A'hearn M et al (2018) Report of the IAU working group on cartographic coordinates and rotational elements: 2015. Celest Mech Dyn Astron 130:1–46

Ashkenazy Y (2019) The surface temperature of Europa. Heliyon 5(6):e01908

Ashkenazy Y, Tziperman E, Nimmo F (2023) Non-synchronous rotation on Europa driven by ocean currents. AGU Adv 4(3):e2022AV000849

Bayer T, Bittner M, Buffington B et al (2019) Europa clipper mission: preliminary design report. In: 2019 IEEE aerospace conference, pp 1–24

Billings SE, Kattenhorn SA (2005) The great thickness debate: ice shell thickness models for Europa and comparisons with estimates based on flexure at ridges. Icarus 177(2):397–412 (**Europa Icy Shell**)

Bills BG (2005) Free and forced obliquities of the Galilean satellites of Jupiter. Icarus 175(1):233–247

Burns JA, Matthews MS et al (1986) Satellites, vol 77. University of Arizona Press, Arizona

Carnahan E, Vance SD, Cox R et al (2022) Surface-to-ocean exchange by the sinking of impact generated melt chambers on Europa. Geophys Res Lett 49(24):e2022GL100287

Carr MH, Belton MJ, Chapman CR et al (1998) Evidence for a subsurface ocean on Europa. Nature 391(6665):363–365

Cassen P, Reynolds RT, Peale S (1979) Is there liquid water on Europa? Geophys Res Lett 6(9):731–734

Collins G, Nimmo F (2009) Chaotic terrain on Europa. Europa pp 259–281

Cook RD et al (2007) Concepts and applications of finite element analysis. Wiley, Oxford

Craft KL, Patterson GW, Lowell RP et al (2016) Fracturing and flow: investigations on the formation of shallow water sills on Europa. Icarus 274:297–313

Culha C, Manga M (2016) Geometry and spatial distribution of lenticulae on Europa. Icarus 271:49–56

Dershowitz W, Mauldon M, Pointe PL (2020) Fracture abundance measures. In: U.S. Rock Mechanics/Geomechanics Symposium, pp ARMA–2020–1586

Figueredo P, Chuang F, Rathbun J et al (2002) Geology and origin of Europa's "Mitten'' feature (Murias Chaos). J Geophys Res Planets 107(E5):1–2

Gammon P, Kiefte H, Clouter M et al (1983) Elastic constants of artificial and natural ice samples by Brillouin spectroscopy. J Glaciol 29(103):433–460

Geissler P, Greenberg R, Hoppa G et al (1998) Evidence for non-synchronous rotation of Europa. Nature 391(6665):368–370

Goodman D (1980) Critical stress intensity factor (KIc) measurements at high loading rates for polycrystalline ice. Physics and Mechanics of Ice: Symposium Copenhagen, August 6–10, 1979. Technical University of Denmark, Springer, pp 129–146

Greeley R, Sullivan R, Klemaszewski J et al (1998) Europa: initial Galileo geological observations. Icarus 135(1):4–24

Greenberg R, Geissler P, Tufts BR et al (2000) Habitability of Europa's crust: the role of tidal-tectonic processes. J Geophys Res Planets 105(E7):17551–17562

Haynes F (1978) Effect of temperature on the strength of snow-ice. CRREL report, Civil Works Directorate and Cold Regions Research and Engineering Laboratory (U.S.)

Helfenstein P, Parmentier E (1983) Patterns of fracture and tidal stresses on Europa. Icarus 53(3):415–430

Hussmann H, Spohn T, Wieczerkowski K (2002) Thermal equilibrium states of Europa's ice shell: implications for internal ocean thickness and surface heat flow. Icarus 156(1):143–151

Jacobson R, Haw R, McElrath T et al (2000) A comprehensive orbit reconstruction for the Galileo prime mission in the J2000 system. J Astronaut Sci 48:495–516

Jaeger JC, Cook NG, Zimmerman R (2007) Fundamentals of rock mechanics. Wiley, Oxford

Kargel JS, Kaye JZ, Head JW III et al (2000) Europa's crust and ocean: origin, composition, and the prospects for life. Icarus 148(1):226–265

Lee S, Pappalardo RT, Makris NC (2005) Mechanics of tidally driven fractures in Europa's ice shell. Icarus 177(2):367–379

Leonard E, Pappalardo R, Yin A (2018) Analysis of very-high-resolution Galileo images and implications for resurfacing mechanisms on Europa. Icarus 312:100–120

Leonard EJ, Howell SM, Mills A et al (2022) Finding order in chaos: quantitative predictors of chaos terrain morphology on Europa. Geophys Res Lett 49(8):e2021GL097309

Liu HW, Miller KJ (1979) Fracture toughness of fresh-water ice. J Glaciol 22(86):135–143

Marshall ST, Kattenhorn SA (2005) A revised model for cycloid growth mechanics on Europa: evidence from surface morphologies and geometries. Icarus 177(2):341–366

Mazars J, Hamon F, Grange S (2015) A new 3d damage model for concrete under monotonic, cyclic and dynamic loadings. Mater Struct 48:3779–3793

McEwen AS (1986) Tidal reorientation and the fracturing of Jupiter's moon Europa. Nature 321(6065):49–51

McKinnon WB (1999) Convective instability in Europa's floating ice shell. Geophys Res Lett 26(7):951–954

Melosh H (1980) Tectonic patterns on a tidally distorted planet. Icarus 43(3):334–337

Moore JM, Asphaug E, Sullivan RJ et al (1998) Large impact features on Europa: results of the Galileo nominal mission. Icarus 135(1):127–145

Nejati M, Paluszny A, Zimmerman RW (2015) A disk-shaped domain integral method for the computation of stress intensity factors using tetrahedral meshes. Int J Solids Struct 69:230–251

Nimmo F (2004) What is the Young's modulus of ice? In: Workshop on Europa's icy shell: past, present, and future, p 7005

Nimmo F, Thomas P, Pappalardo R et al (2007) The global shape of Europa: constraints on lateral shell thickness variations. Icarus 191(1):183–192

Office USNONA, Office GBNA, Science et al (2016) The Astronomical Almanac for the Year ... U.S. Government Printing Office

Ojakangas GW, Stevenson DJ (1989) Thermal state of an ice shell on Europa. Icarus 81(2):220–241

Paluszny A, Zimmerman RW (2013) Numerical fracture growth modeling using smooth surface geometric deformation. Eng Fract Mech 108:19–36

Pappalardo RT, Belton MJ, Breneman H et al (1999) Does Europa have a subsurface ocean? Evaluation of the geological evidence. J Geophys Res Planets 104(E10):24015–24055

Paris P, Erdogan F (1963) A critical analysis of crack propagation laws. J Basic Eng 85(4):528–533

Petrovic J (2003) Review mechanical properties of ice and snow. J Mater Sci 38:1–6

Pierce M (2017) An introduction to random disk discrete fracture network (DFN) for civil and mining engineering applications. ARMA e-Newslett 20:3–8

Poinelli M, Larour E, Castillo-Rogez J et al (2019) Crevasse propagation on brittle ice: application to cycloids on Europa. Geophys Res Lett 46(21):11756–11763

Qin R, Buck WR, Germanovich L, (2007) Comment on "Mechanics of tidally driven fractures in Europa's ice shell" by S. Lee, RT Pappalardo, and NC Makris, (2005) Icarus 177, 367–379]. Icarus 189(2):595–597

Rhoden AR, Hurford TA (2013) Lineament azimuths on Europa: implications for obliquity and non-synchronous rotation. Icarus 226(1):841–859

Rhoden AR, Militzer B, Huff EM et al (2010) Constraints on Europa's rotational dynamics from modeling of tidally-driven fractures. Icarus 210(2):770–784

Rhoden AR, Hurford TA, Manga M (2011) Strike-slip fault patterns on Europa: obliquity or polar wander? Icarus 211(1):636–647

Richard H, Fulland M, Sander M (2005) Theoretical crack path prediction. Fatig Fract Eng Mater Struct 28(1–2):3–12

Richard H, Schramm B, Schirmeisen NH (2014) Cracks on mixed mode loading-theories, experiments, simulations. Int J Fatig 62:93–103

Rudolph ML, Manga M (2009) Fracture penetration in planetary ice shells. Icarus 199(2):536–541

Saceanu MC, Paluszny A, Zimmerman RW et al (2022) Fracture growth leading to mechanical spalling around deposition boreholes of an underground nuclear waste repository. Int J Rock Mech Min Sci 152:105038

Schenk PM (2002) Thickness constraints on the icy shells of the Galilean satellites from a comparison of crater shapes. Nature 417(6887):419–421

Schmidt B, Blankenship D, Patterson G et al (2011) Active formation of 'chaos terrain' over shallow subsurface water on Europa. Nature 479(7374):502–505

Schulze-Makuch D, Irwin LN (2001) Alternative energy sources could support life on Europa. EOS Trans Am Geophys Union 82(13):150–150

Sinha NK (1989) Elasticity of natural types of polycrystalline ice. Cold Reg Sci Technol 17(2):127–135

Thomas RN, Paluszny A, Zimmerman RW (2020) Growth of three-dimensional fractures, arrays, and networks in brittle rocks under tension and compression. Comput Geotech 121:103447

Trumbo SK, Brown ME (2023) The distribution of co₂ on europa indicates an internal source of carbon. Science 381(6664):1308–1311

Van Hoolst T, Rambaux N, Karatekin Ö et al (2008) The librations, shape, and icy shell of Europa. Icarus 195(1):386–399

Vilella K, Choblet G, Tsao WE et al (2020) Tidally heated convection and the occurrence of melting in icy satellites: application to Europa. J Geophys Res Planets 125(3):e2019JE006248

Wahr J, Selvans ZA, Mullen ME et al (2009) Modeling stresses on satellites due to nonsynchronous rotation and orbital eccentricity using gravitational potential theory. Icarus 200(1):188–206

Walker CC, Bassis JN, Schmidt BE (2021) Propagation of vertical fractures through planetary ice shells: the role of basal fractures at the ice-ocean interface and proximal cracks. Planet Sci J 2(4):135

Publisher's Note Springer Nature remains neutral with regard to jurisdictional claims in published maps and institutional affiliations.